ADVANCED OPTICAL MATERIALS

www.advopticalmat.de

Pairing Toroidal and Magnetic Dipole Resonances in Elliptic Dielectric Rod Metasurfaces for Reconfigurable Wavefront Manipulation in Reflection

Odysseas Tsilipakos, Anna C. Tasolamprou, Thomas Koschny, Maria Kafesaki, Eleftherios N. Economou, and Costas M. Soukoulis*

A novel approach for reconfigurable wavefront manipulation with gradient metasurfaces based on permittivity-modulated elliptic dielectric rods is proposed. It is shown that the required 2π phase span in the local electromagnetic response of the metasurface can be achieved by pairing the lowest magnetic dipole Mie resonance with a toroidal dipole Mie resonance, instead of using the lowest two Mie resonances corresponding to fundamental electric and magnetic dipole resonances as customarily exercised. This approach allows for the precise matching of both the resonance frequencies and quality factors. Moreover, the accurate matching is preserved if the rod permittivity is varied, allowing for constructing reconfigurable gradient metasurfaces by locally modulating the permittivity in each rod. Highly efficient tunable beam steering and beam focusing with ultrashort focal lengths are numerically demonstrated, highlighting the advantage of the low-profile metasurfaces over bulky conventional lenses. Notably, despite using a matched pair of Mie resonances, the presence of an electric polarizability background allows to perform the wavefront shaping operations in reflection, rather than transmission. This has the advantage that any control circuitry necessary in an experimental realization can be accommodated behind the metasurface without affecting the electromagnetic response.

1. Introduction

Metasurfaces have attracted considerable attention in recent years due to their ability to control light across their deeply subwavelength thickness. The numerous applications envisioned span a vast range including perfect absorption,[1] electromagnetically induced transparency,[2] wavefront transformations,[3] dispersion compensation,[4] nonreciprocal response,[5] ultrathin laser sources,[6] and broadband tunable group delay.[7]

All-dielectric versions of metasurfaces are particularly interesting since they can manipulate light with minimal dissipative losses.[8] They are typically formed by arranging subwavelength dielectric particles on a flat surface. By ensuring that the particles support perpendicular electric and magnetic resonances so that they can be accessed with the same plane wave, we can achieve unidirectional scattering—a direct generalization of the Kerker conditions.[9] For operation in transmission one typically relies on a pair of matched electric dipole (ED) and magnetic dipole (MD) resonances, leading to high transmission and an underlying 2π phase shift across the resonance bandwidth.[10] This can be exploited for constructing gradient metasurfaces by introducing a phase gradient along the surface, allowing by Huygens' principle for arbitrary wavefront manipulation operations.[11–14] In elementary particle shapes, such as spheres, the fundamental ED and MD resonances are spectrally separated. As a result, an extra degree of freedom is typically required for making them overlap. For example, this can be the height in dielectric disks;[10] other approaches include dielectric cut-wires,[15] disks with an etched center region,[16] and C-shaped particles.[17] Through proper design, diverse functionalities have been demonstrated: perfect absorption,[18] beam steering and focusing,[10,16,17] polarization control,[15,19] electromagnetically-induced transparency,[20] and holography.[21]

In this work, we focus on metasurfaces made of cylindrical dielectric rods, which are uniform along their axis and correspond to 2D instead of 3D particles (e.g., disks). Relying on 2D particles can lead to easier addressing of each meta-atom (i.e., local instead of global tunability[22]), allowing for implementing multiple functions with the same metasurface design. We thus demonstrate reconfigurable wavefront

Dr. O. Tsilipakos, Dr. A. C. Tasolamprou, Dr. M. Kafesaki, Prof. E. N. Economou, Prof. C. M. Soukoulis
Institute of Electronic Structure and Laser
FORTH
GR-71110 Heraklion, Crete, Greece
E-mail: otsilipakos@iesl.forth.gr

Dr. T. Koschny, Prof. C. M. Soukoulis
Ames Laboratory—U.S. DOE and Department of Physics and Astronomy
Iowa State University
Ames, IA 50011, USA

Dr. M. Kafesaki
Department of Materials Science and Technology
University of Crete
GR-71003 Heraklion, Crete, Greece

Prof. E. N. Economou
Department of Physics
University of Crete
GR-71003 Heraklion, Crete, Greece

The ORCID identification number(s) for the author(s) of this article can be found under https://doi.org/10.1002/adom.201800633.

DOI: 10.1002/adom.201800633

manipulation inside the incidence plane by locally tuning the permittivity of each rod. As is the case with spheres, ED and MD resonances in rods of circular cross-section do not overlap. We thus introduce an extra degree of freedom, namely, an elliptical cross-section. Instead of focusing on the lowest-order electric resonance as customarily exercised, we demonstrate that it is possible to align a toroidal dipole (TD) resonance with the fundamental MD resonance. The TD resonance is of electric nature and can be viewed as a higher-order electric resonance with a dipolar radiation pattern. We demonstrate precise matching of the two resonances in both frequency and quality factor, illustrating that in this respect the TD resonance is more compatible with the MD resonance than the fundamental ED resonance. In addition, we show that the resonances remain matched (frequency and quality factor) while varying the meta-atom size and, more importantly, the rod permittivity. The latter allows for constructing tunable gradient metasurfaces by employing, e.g., ceramic materials. The proposed concept is schematically illustrated in **Figure 1**.

To demonstrate the potential of the proposed metasurfaces, we focus on two typical wavefront shaping operations: we demonstrate tunable beam steering with very high efficiencies and, in addition, we show tunable beam focusing targeting ultrashort focal lengths to highlight the advantage of our low-profile focusing metasurfaces over bulky conventional lenses based on phase accumulation. Notably, the wavefront shaping operations are conducted in reflection instead of transmission, something that is advantageous in the context of reconfigurable metasurfaces since any control circuitry can

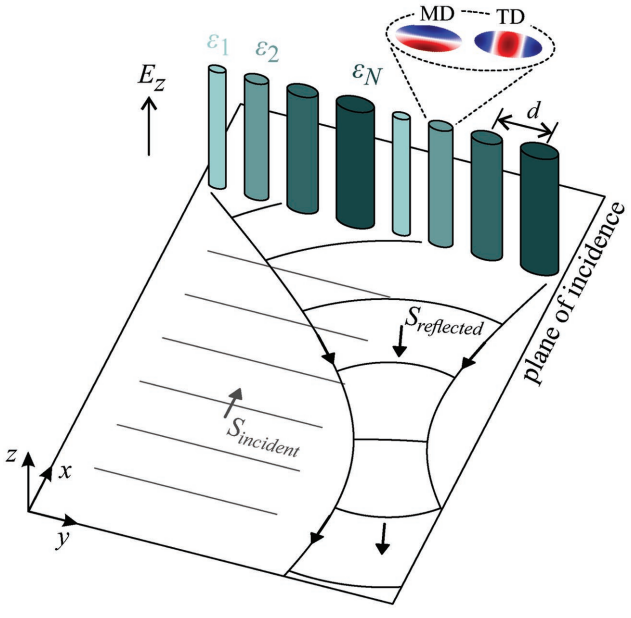

Figure 1. Elliptic dielectric rod gradient metasurface performing beam steering and focusing inside the *xy*-incidence plane. Curved lines represent the wavefronts, and arrows indicate the energy flow (time-averaged Poynting vector $\boldsymbol{S}$). The size or permittivity of each meta-atom is properly modified to implement the required phase profile. The 2π phase span is supplied by the two matched magnetic dipole (MD) and toroidal dipole (TD) resonances.

be accommodated behind the metasurface without interfering with the electromagnetic wave. This is an initially counterintuitive result since we have relied on a pair of matched resonances. As thoroughly explained in Section 4.1, it is due to an electric polarizability background, illustrating that it is not always safe to assume that matched resonances result in perfect transmission.

2. Mie Resonances in Elliptic Dielectric Rod Meta-Atoms

We start with the Mie resonances supported by a single cylindrical uniform (i.e., infinitely long) dielectric rod. In particular, we are interested in the evolution of the supported resonances as the eccentricity of the rod cross-section is varied. We focus on the transverse electric (TE) polarization ($\boldsymbol{E} \equiv E_z\hat{\boldsymbol{z}}$, along the rod axis) and start from a circular cross-section. The four lowest-order Mie resonances are presented in **Figure 2**a along with the corresponding resonant frequencies, f, and quality factors, Q. They have been calculated for a radius $r = 8\,\mu$m and a permittivity $\varepsilon_r = 41$, corresponding to $LiTaO_3$ at low terahertz frequencies far below the phonon resonances to minimize absorption,[23] assuming a wavevector in the xy-plane ($k_z = 0$). Color refers to the polarization current $J_z = j\omega\varepsilon_0(\varepsilon_r - 1)E_z$ and arrows to the magnetic field that lies in the xy-plane exclusively ($\boldsymbol{H} \equiv \boldsymbol{H}_{\parallel}$). Note that quality factors refer to radiation losses, since for discussing the resonances, the adopted permittivity is purely real. The four modes are denoted as TE_{pq}, where subscript p refers to the azimuthal and q to the radial order. Modes TE_{00} and TE_{10} are the fundamental electric and magnetic dipole resonances, respectively. They are characterized by perpendicular dipole moments (p_z and m_y) and could be in principle exploited for constructing Huygens' metasurfaces. However, they are significantly separated in frequency, as is the case with fundamental ED and MD resonances in spheres, and also differ significantly in their quality factors.

We now make the cross-section elliptical and let the major to minor semiaxis ratio $\gamma = a/b$ vary while maintaining the cross-sectional area constant ($\pi ab = \pi r^2 = 64\pi\,\mu m^2$). The major and minor semiaxes scale as $a = r\sqrt{\gamma}$ and $b = r/\sqrt{\gamma}$ where $r = 8\,\mu$m. The ratio γ ($\gamma \geq 1$) is associated with the eccentricity through $e = \sqrt{1-\gamma^{-2}}$ ($0 \leq e < 1$). We want to investigate whether modes of electric and magnetic nature can be made to overlap in frequency. As soon as the cross-section becomes elliptical ($\gamma \neq 1$), the continuous rotational symmetry breaks, leading to frequency splitting for the resonances of nonzero azimuthal order: TE_{10} and TE_{20}. As a result, for the elliptic rod we get six resonances out of the four modes depicted in Figure 2a. Their resonant frequencies are depicted in Figure 2b as a function of the semiaxis ratio γ. Resonance TE_{00} (TE_{01}) is of electric nature but evolves toward even lower (higher) resonant frequencies and thus does not offer the possibility of overlapping with a resonance of magnetic nature. We thus focus on the four resonances stemming from modes TE_{10} and TE_{20} labeled $TE_{10}^{+/-}$ and $TE_{20}^{+/-}$ to indicate frequency splitting to higher or lower frequencies. Since the continuous rotational symmetry has been reduced to C_2 discrete rotational symmetry, the modes can

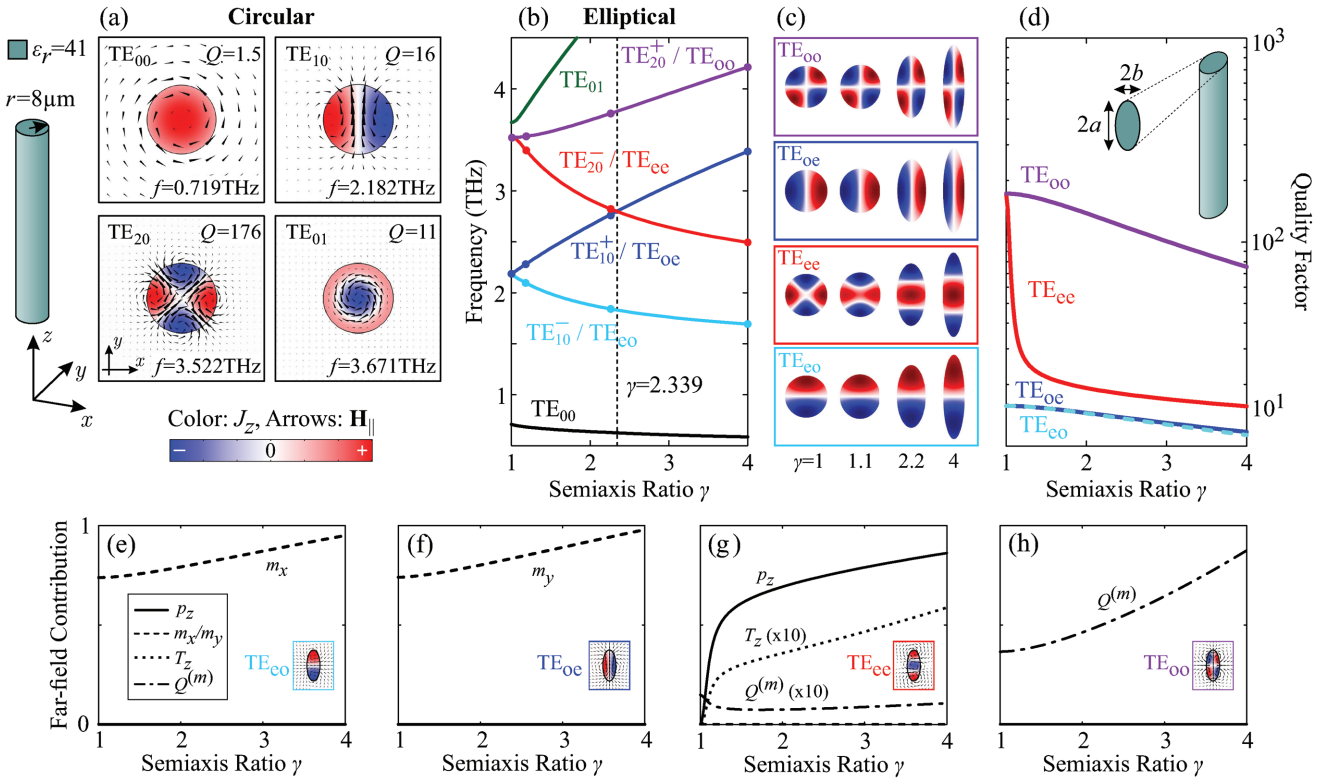

Figure 2. a) First four Mie resonances of TE polarization ($\boldsymbol{E} \equiv E_z\hat{\boldsymbol{z}}$) for an infinitely long rod of circular cross-section with $\varepsilon_r = 41$ and $r = 8$ μm. Modes are labeled according to their azimuthal and radial orders. b–d) Evolution of Mie resonances in an elliptic dielectric rod as the eccentricity varies. (b) Resonant frequencies as a function of semiaxis ratio $\gamma = a/b$. TE_{oe} (MD) and TE_{ee} (TD) resonances align for $\gamma = 2.339$. (c) Evolution of mode profiles for characteristic values of γ marked in (b). (d) Quality factors as a function of semiaxis ratio. e–h) Far-field contribution of each multipole as a function of γ. TE_{eo} (e) and TE_{oe} (f) are preserved magnetic dipoles and TE_{oo} (h) is a preserved magnetic quadrupole. TE_{ee} (g) starts off as pure magnetic quadrupole and acquires a strong electric dipole moment. It is uniquely characterized by the toroidal dipole moment.

no longer be conveniently classified in terms of their angular momentum. As a result, we adopt a classification in terms of even (e) or odd (o) symmetry with respect to the axes of the ellipse (coinciding with the Cartesian axes x and y). This is also consistent with the subsequent extension from the meta-atom to the metasurface.

The evolution of the mode profiles with increasing eccentricity is shown in Figure 2c for characteristic values of the semiaxis ratio γ marked in Figure 2b. Modes TE_{eo}, TE_{oe}, and TE_{oo} evolve in a rather trivial manner; their character is preserved as the eccentricity varies due to mode topology. Specifically, modes TE_{eo}, and TE_{oe} are preserved magnetic dipoles (m_x and m_y, respectively), while mode TE_{oo} is a preserved magnetic quadrupole. Being odd functions at least along one of the two axes, they cannot acquire an electric dipole moment. In stark contrast, TE_{ee} starts off as a magnetic quadrupole but acquires an electric dipole moment as the eccentricity varies. This is possible since it is even along both axes. Notably, for $\gamma = 2.339$ mode TE_{ee} aligns in frequency with mode TE_{oe} which is of magnetic dipole nature, thus offering the possibility for matching perpendicular resonances of electric (p_z) and magnetic (m_y) nature.

To corroborate the above observations based on mode profile inspection, we perform a multipole expansion on the polarization current distributions of the eigenmodes using the expressions found in ref. [24] and subsequently assess the far field contribution of each moment by azimuthally integrating the resulting power density. The results are depicted in Figure 2e–h, where we plot the far field contribution of electric dipole (p_z), magnetic dipole (m_x or m_y), toroidal dipole (T_z), and magnetic quadrupole ($Q^{(m)}$) moments for the four eigenmodes under investigation. One can readily verify the preserved magnetic dipole nature of modes TE_{eo}, TE_{oe}, and the preserved magnetic quadrupole nature of mode TE_{oo}. Mode TE_{ee} starts off as a pure magnetic quadrupole, with only $Q^{(m)}$ being nonzero for $\gamma = 1$. However, as γ increases, it acquires a strong electric dipole moment. In addition, it is characterized by a toroidal dipole moment (Figure 2g); the respective contribution is magnified by a factor of 10. The TD moment stems from a specific distribution of polarization/conduction currents.[25–28] A pure toroidal dipole moment is characterized by currents flowing on the surface of a 3D torus, giving rise to a confined magnetic field vortex. A ring-like magnetic field distribution threading displacement current loops formed by antiparallel polarization currents flowing in the center and outer part of the ellipse is clearly visible in the TE_{ee} mode distribution. However, being only an approximation of the archetypical toroidal configuration, mode TE_{ee} features also magnetic quadrupole (magnified by a factor of 10) and, predominantly, electric dipole contributions (Figure 2g). Since the presence of the T_z moment is

unique to the TE_{ee} mode, we term it a TD resonance; however, one should keep in mind that it is the electric dipole moment that dominates.

Having studied the multipole expansion, we discuss the radiative quality factors depicted in Figure 2d. For $\gamma = 1$, modes TE_{ee} and TE_{oo} as magnetic quadrupoles are far less radiative than modes TE_{oe} and TE_{eo} which are magnetic dipoles. As γ increases, mode TE_{ee} becomes much more radiative approaching the radiation damping of the magnetic dipoles. This is because it acquires a strong electric dipole moment (Figure 2g). On the other hand, mode TE_{oo} remains a pure magnetic quadrupole and the quality factor does not decrease considerably.

To recapitulate, using an elliptical cross-section and the resulting frequency splitting, we succeeded in aligning the resonant frequencies of the fundamental MD resonance and a TD resonance (instead of the fundamental ED resonance as customarily exercised). The TD resonance is characterized by a strong electric dipole moment and a dipolar far-field radiation pattern. As a result, the two resonances can be exploited for achieving unidirectional scattering. Another strategy for matching such resonances is to utilize coupled-rod metamolecules.[29] Notice that that the respective quality factors are not equal, i.e., for $\gamma = 2.339$, we find $Q_{ee} = 18$ and $Q_{oe} = 14$. Our next concern is to construct a metasurface from the elliptical meta-atoms and match the corresponding collective resonances in both frequency and quality factor.

3. Elliptic Rod Metasurfaces: Simultaneously Matching Frequencies and Quality Factors

The metasurface under study is comprised of elliptic rods periodically arranged along the y-axis with a pitch (lattice constant) equal to d (see inset in **Figure 3**b). The metasurface supports collective eigenmodes (indicated with a prime) which are modified with respect to their single meta-atom counterparts due to interatom coupling. They are calculated through an eigenvalue simulation of the unit cell performed with the commercial electromagnetic software COMSOL Multiphysics which implements the vectorial finite element method.[30,31] We obtain access to all the eigenmodes supported by the structure and more specifically their eigenvalue (complex resonant frequency) and eigenvector (mode profile). Periodic boundary conditions are implemented on the xz-planes to model the periodic arrangement of the meta-atoms along the y-axis. The phase delay between the two xz-planes is set to zero, since we are seeking the eigenmodes that can be excited when impinging at normal incidence ($k_y = 0$). In the yz limits of the bounding box, we implement absorbing boundary conditions. This is necessary since the modes of interest exhibit significant radiation leakage, which should be absorbed without reflections in order to obtain a correct solution.

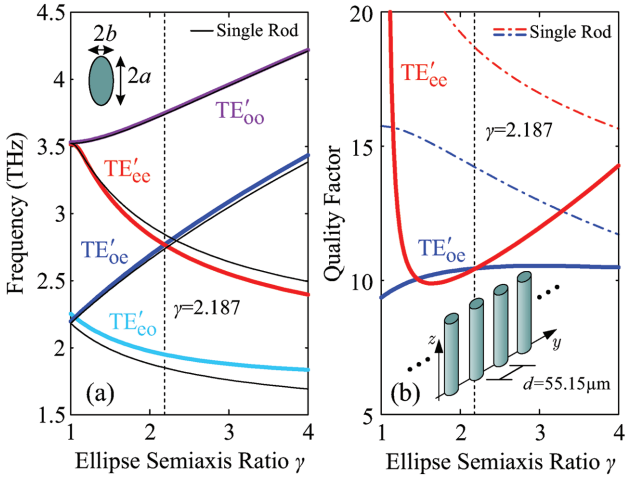

Figure 3. Metasurface made of elliptical rods with a pitch $d = 55.15$ μm. Evolution of TE-polarization collective resonances as the eccentricity varies. a) Resonant frequencies and b) quality factors as a function of the semiaxis ratio $\gamma = a/b$. TE'_{oe} (MD) and TE'_{ee} (TD) resonances match in frequency and quality factor for $\gamma = 2.187$.

For a pitch $d = 55.15$ μm, the evolution of collective modes TE'_{eo}, TE'_{oe}, TE'_{ee}, and TE'_{oo} with the semiaxis ratio γ is depicted in Figure 3a. The resonant frequencies of the collective modes do not deviate significantly from their single-atom counterparts; the deviation is most noticeable for modes TE'_{eo} and TE'_{ee} which is to be anticipated given the local near-field patterns (see Figure 2c). As in Figure 2a, there is a γ value for which f'_{eo} and f'_{ee} meet (2.187 in this case instead of 2.339). The respective quality factors are shown in Figure 3b. Unlike the resonant frequencies, they deviate noticeably from the single-atom counterparts. As a result, in contrast to the meta-atom case (Figure 2d), here there is a γ value for which Q'_{oe} and Q'_{ee} do meet. In fact, for the value $d = 55.15$ μm we have selected, the intersection point for quality factors coincides with the intersection point for resonant frequencies. Note that modes TE'_{eo} and TE'_{oo} are dark to a normally incident plane wave since they are antisymmetric with respect to the xz-mirror plane. Therefore, their radiation quality factors are infinite and thus not seen in Figure 3b.

The pitch value of $d = 55.15$ μm was judiciously chosen so that MD (TE'_{oe}) and TD (TE'_{ee}) resonances can match in both frequency and quality factor for an appropriate value of γ. For different pitch values, this is in general not possible. For example, for $d = 70$ μm f's and Q's do meet but for a different γ value, whereas for $d = 50$ μm, the quality factors do not meet at all (see the Supporting Information). The optimum pitch value was found by performing a thorough parametric analysis in terms of both d and γ (**Figure 4**). In Figure 4a, we plot $\Delta f = f'_{oe} - f'_{ee}$. As already seen in Figure 3a, f'_{oe} increases with γ, whereas f'_{ee} decreases. The crossing between them ($\Delta f = 0$ contour) is marked with a solid line. Note that it is almost vertical, indicating that the resonant frequencies only slight depend on the pitch value. The difference in quality factors $\Delta Q = Q'_{oe} - Q'_{ee}$ is plotted in Figure 4b. Two regimes can be identified. For small γ values, ΔQ mainly depends on the semiaxis ratio. However, for higher γ values, ΔQ becomes pitch-dependent. The $\Delta Q = 0$ contour (solid line) becomes horizontal, guaranteeing a crossing with the $\Delta f = 0$ contour (dashed line). This behavior of ΔQ is inherited from Q'_{ee}, as Q'_{oe} does not vary considerably with pitch or ratio.

The procedure of matching the MD and TD resonances in elliptic rod metasurfaces is not limited to a specific dielectric material. This is demonstrated in **Table 1** where we compile the required geometric parameters and the resulting common

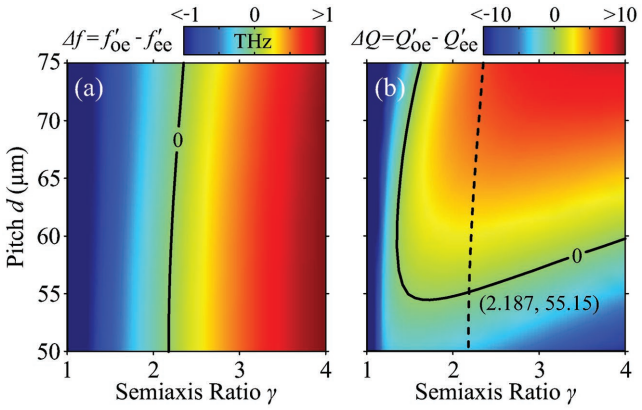

Figure 4. Parametric analysis plots. a) $\Delta f = f'_{oe} - f'_{ee}$ as a function of metasurface pitch d and meta-atom semiaxis ratio γ. The $\Delta f = 0$ contour is marked with a solid line. b) $\Delta Q = Q'_{oe} - Q'_{ee}$ as a function of metasurface pitch d and meta-atom semiaxis ratio γ. The $\Delta Q = 0$ contour is marked with a solid line. The two contours cross for the parameter combination ($\gamma = 2.187$, $d = 55.15$ μm).

resonant frequencies/quality factors for different permittivity values. Here, we have focused on ferroelectric ceramic materials that can supply high permittivity values in the gigahertz frequency range and have tuned the ellipse dimensions accordingly. For example, $Ba_{0.5}Sr_{0.5}TiO_3$ (BST-0.5) can supply the permittivity of 600 at microwave frequencies and has been successfully utilized for demonstrating dielectric metamaterials.[32] Increasing the permittivity results in higher quality factors for the matched resonances and, furthermore, renders the pitch (meta-atom spacing) more subwavelength. Both of these traits are beneficial for designing gradient metasurfaces. For example, the shorter the pitch, the finer the discretization of the required phase profile. Even more importantly, ferroelectric materials feature a strong dependence of the permittivity on external stimuli, such as temperature or an applied electric field.[33,34] This is essential for constructing reconfigurable gradient metasurfaces by locally tuning the permittivity of each constituent rod. Specifically, BST-0.5 features ample tunability of 15% around the rest permittivity of 600 for moderate electric field strengths.[34]

4. Reflective Gradient Dielectric Rod Metasurfaces

We can now exploit the matched MD and TD resonances for constructing gradient metasurfaces and performing arbitrary wavefront manipulation operations. This is schematically illustrated in Figure 1 where by locally modulating the permittivity or size of the constituent elliptic dielectric rods, we steer and focus the impinging radiation. Henceforth, we focus on BST-0.5 metasurfaces that support matched MD and TD resonances at 20 GHz (Table 1). The loss tangent is initially set to $\tan\delta = 10^{-4}$.

Table 1. Frequencies and quality factors of matched MD and TD resonances in elliptic dielectric rod metasurfaces with different permittivity values. The required geometric parameters (elliptical cross-section and pitch) are included.

	$\varepsilon_r = 41$	$\varepsilon_r = 200$	$\varepsilon_r = 600$
$f'_{ee} = f'_{oe}$	2.767 THz	20.2 GHz	20 GHz
$Q'_{ee} = Q'_{oe}$	10	24	43
a	11.83 μm	0.744 mm	0.435 mm
b	5.41 μm	0.336 mm	0.196 mm
d	55.15 μm ($\sim\lambda_0/2$)	3.85 mm ($\sim\lambda_0/4$)	2.31 mm ($\sim\lambda_0/7$)

4.1. Perfect Reflection with Matched Resonances

The spectral response of the uniform metasurface is depicted in **Figure 5**a. In the neighborhood of 20 GHz where the resonance pair acts we obtain an almost featureless, constant amplitude response with an underlying 2π phase modulation (inset). Interestingly, we do not get perfect transmission, as anticipated for matched resonances,[10] but, rather, perfect reflection. This is an atypical and initially counterintuitive result. It can be explained by observing the response across a wider spectral range. Specifically, it can be readily seen that there is high reflection from low frequencies that is due to the electric polarizability background. This is verified by plotting the reflection and transmission scattering coefficients for a filling factor–equivalent dielectric slab. The slab thickness is $t = \pi ab/d = 0.116$ mm as found by substituting from Table 1.

In Figure 5b, we plot the reflected power from the electric (p_z), magnetic (m_y), and toroidal (T_z) dipole moment. The power scattered by T_z is much smaller than the other two contributions and is shown magnified by a factor of 200; it mainly serves to identify the excitation of the TD resonance being unique to that particular eigenmode (see Figure 2). Note that since the multipole expansion is performed on the induced polarization current and not the far-field pattern, we are able to distinguish the different multipole contributions even if they are indistinguishable in terms of the angular momentum of their radiation (due to the periodic nature of the structure), or even the parity characteristics of the plane-wave scattered field. In addition, it should be noted that besides the power scattered individually by the electric and the magnetic dipole moment shown in Figure 5b, there is also an interference power term; however, in our case, it is negligible since in the spectral regions were both p_z and m_y are nonzero, the respective scattered fields have a phase difference of $\pm\pi/2$. Returning to Figure 5b, the polarizability background results in a strong, broad p_z contribution, leading to almost unity reflection. At the vicinity of 20 GHz, the TD resonance is excited as verified by the peaking of T_z. It is accompanied by a strong electric dipole moment (Figure 2g), resulting in a p_z incision. No power at all would be scattered by the metasurface at 20 GHz if it was not for the MD resonance that is excited at the same frequency and leads to a sharp peak in the power scattered by the m_y dipole moment. By aligning the TD and MD resonant frequencies, we have centered the p_z incision with the m_y peak and by matching the quality factors, we have equated the linewidths. If either frequencies or quality factors deviate from being equal through a different choice of semiaxis ratio or pitch, the featureless amplitude response is lost (see the Supporting Information).

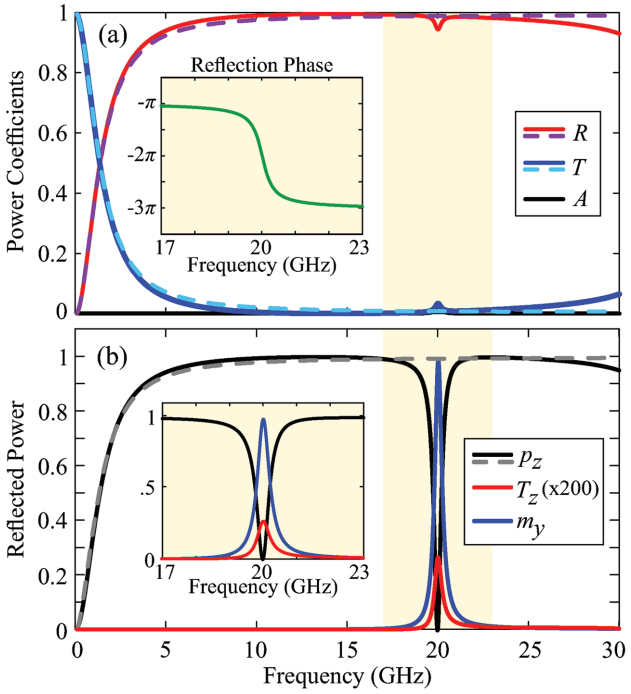

Figure 5. Uniform metasurface made out of BST-0.5 ($\varepsilon_r = 600$) with the geometric parameters in Table 1. a) *R*, *T*, *A* scattering coefficients and reflection phase (inset). Around 20 GHz, we get flat response and an underlying 2π shift due to the two resonances. Reflection is high from lower frequencies due to the electric polarizability background. Dashed curves correspond to the filling factor–equivalent slab (thickness $t = \pi ab/d = 0.116$ mm). b) Power scattered by the electric, magnetic, and toroidal dipoles. The polarizability background results in a broad p_z contribution. At 20 GHz, we see an incision in p_z due to the excitation of the TD resonance and a peak in m_y due to the excitation of the MD resonance.

In Figure 5a, we have obtained a 2π phase modulation under high reflection by two matched electric and magnetic resonances plus an electric polarizability background (essential for switching from transmission to reflection). It should be noted that if it was not for this background, two resonances are not adequate for obtaining a 2π modulation under high reflection: arranging an electric and a magnetic resonance side by side as in refs. [35,36] produces a high-reflection band over their aggregate bandwidth but does not give access to the entire 2π phase under high reflection, so as to be exploited for wavefront manipulation. In fact, interleaving three resonances (electric–magnetic–electric or vice-versa) is necessary for obtaining the 2π shift under high reflection.[7] Other approaches to the same problem are utilizing a metallic backplane[37,38] or magnetoelectric coupling.[39] Compared to structures with a metallic backplane, our approach does not preclude transmission altogether. By detuning the two resonances, spectral regions of high transmission can be opened (see Figure S4 in the Supporting Information), something that may be desirable for specific applications. In addition, another application scenario that is uniquely suited to our approach is locally tunable gradient metasurfaces in the terahertz regime where the customary choice of introducing varactors in metal-based metasurfaces is very challenging.

4.2. Tuning with Permittivity

In order to construct gradient metasurfaces based on the matched resonance pair, the resonances should remain matched when varying the permittivity or size. Here, we focus on permittivity modulation to allow for reconfigurable operation. When varying the rod permittivity, the TD and MD resonances considered in this work remain matched in both frequency and quality factor (see the Supporting Information). As a result, the amplitude response remains featureless, but the underlying phase modulation is shifted to a different center frequency (see the Supporting Information). Sitting at a specific frequency (20 GHz) we can access different reflection phases under near-unity reflection (**Figure 6**). Importantly, the ample tunability of BST-0.5 allows for accessing almost the entire 2π shift. Specifically, by assuming that the permittivity can vary inside $\varepsilon_r \in [550, 650]$ (i.e., ≈±8% around 600), we access a span of 300° in reflection phase (inset). Figure 6 constitutes the look-up table for constructing gradient metasurfaces based on permittivity tuning of the elliptic rods. An entirely analogous look-up table for the rod size *r* (keeping γ constant) can be found in the Supporting Information.

4.3. Steering Metamirror

We first demonstrate steering of a plane wave inside the incidence plane ($x\gamma$). For this purpose, we construct a supercell of *N* meta-atoms having a total extent $D = Nd$ along the γ-axis. Imposing a linear reflection phase profile $\varphi_r(\gamma) = \varphi_0 + m(2\pi/D)\gamma$ along the supercell (φ_0 is an arbitrary constant phase), we can deflect the incident wave to the desired direction by promoting a single diffraction order *m*. Simply put, we are constructing the surface analog of a blazed grating. The reflection angle θ_r is determined by momentum conservation: $m(2\pi/D) = k_0[\sin(\theta_r) - \sin(\theta_i)]$. Focusing on normal incidence and working with the first diffraction order we arrive at $\theta_r = \arcsin(\lambda_0/D)$. In our case, the pitch *d* is fixed by the design process for achieving $Q'_{oe} = Q'_{ee}$ (see Figure 4b). Thus, we can select the desired reflection angle by varying the number of meta-atoms comprising the unit cell. Note that relying on a single diffraction order results in

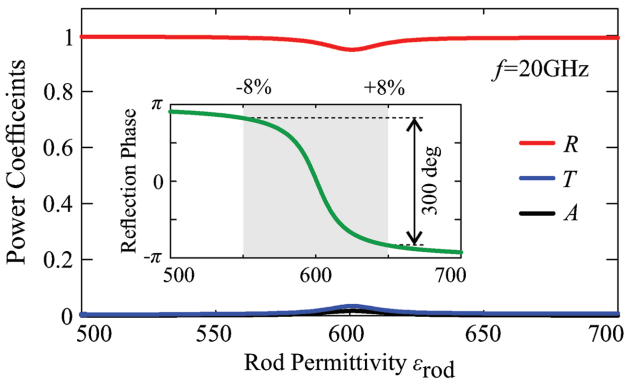

Figure 6. Response of uniform metasurface ($a = 0.435$ mm, $b = 0.196$ mm, $d = 2.31$ mm) to a normally incident plane wave. Reflection amplitude and phase at $f = 20$ GHz as a function of rod permittivity. For $\varepsilon_r \in [550, 650]$, we access a reflection phase span of 300°.

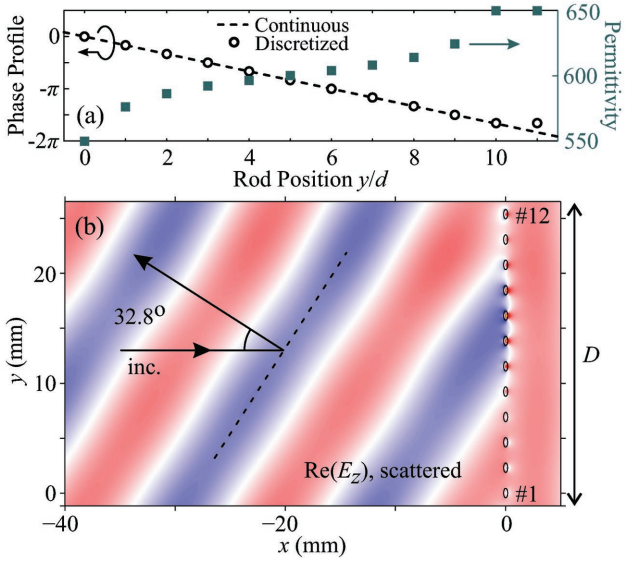

Figure 7. Permittivity-modulated gradient metasurface (a = 0.435 mm, b = 0.196 mm, d = 2.31 mm, N = 12) for anomalous reflection to $\theta_r = 32.8°$. a) Required phase profile and rod permittivities. b) Scattered electric field showing anomalous reflection toward the desired direction.

discrete reflection angles; however, we can achieve a quasicontinuous coverage of reflection angles by implementing phase profiles that cover integer multiples of 2π (wrapped) to promote higher diffraction orders (see the Supporting Information). Our approach of manipulating the diffraction orders of a metasurface supercell is fundamentally different from scanning mirrors or paired wedge (Risley) prisms; however, the end result, i.e., the ability to dynamically control the reflection angle, is the same.

As an example, we set N = 12 corresponding to a reflection angle of 32.8°. The continuous and discretized required phase profile is depicted in **Figure 7**a. By invoking the look-up table of Figure 6, we can specify the required rod permittivities (Figure 7a). The last point in the discretized phase profile deviates slightly from the prescribed value. This is because we have allowed for a finite range of permittivities resulting in a reflection phase span of 300°, which is smaller than the ideally required $2\pi(N-1)/N$. However, as we will see in what follows, this is not detrimental to the performance.

The structure is illuminated with a normally incident plane wave (f = 20 GHz) and the scattered field (E_z) is depicted in Figure 7b. The reflected wavefronts are tilted to the desired angle and are nicely planar indicating complete reflection to the desired diffraction order. To quantify the performance, we assign one port for each diffraction order and calculate the reflected, transmitted, and absorbed power (**Table 2**). 97.1% of the incident power is reflected to the desired diffraction order (m = 1) with only 0.8% lost to the other reflected diffraction orders (m = 0, − 1 are propagating since $D = 12d = 27.6\ \text{mm} \approx 1.85\lambda_0$). Finally, 1.2% is transmitted and 1% is absorbed through Joule losses.

So far, we have considered an optimistic loss tangent of $\tan\delta = 10^{-4}$. In Table 2, we assess the performance for less demanding loss tangent values. The absorbed power obviously increases; however, it is important to note that the remaining

Table 2. Reflected, transmitted, and absorbed power in the steering gradient metasurface for different values of loss tangent. The FOM is defined as $R_{(m=1)}/(1-A)$; in all cases, power is reflected almost exclusively to the desired order.

Power [%]	$\tan\delta = 10^{-4}$	$\tan\delta = 10^{-3}$	$\tan\delta = 10^{-2}$
Reflected (m = 1)	97.1	89.2	41.5
Reflected (rest)	0.8	0.8	3
Transmitted (all)	1.2	0.6	0.3
Absorbed	1	9.4	55.2
FOM	0.98	0.98	0.93

power is almost exclusively reflected to the desired diffraction order. This is highlighted by defining a figure of merit (FOM) according to FOM = $R_{(m=1)}/(1-A)$. As can be seen in the last row of Table 2, in all cases, the FOM is exceptionally high. Resorting to eigenvalue simulations, we have verified that this is because the quality factors Q'_{oe}, Q'_{ee} decrease in unison as the loss tangent increases, i.e., they remain matched.

The number of meta-atoms N can be varied to cover a broad range of reflection angles. Additional examples exploring the limits of this approach can be found in the Supporting Information. Specifically, when N decreases too much, the phase profile discretization becomes coarser and neighboring meta-atoms become quite dissimilar. This strains the periodic approximation under which the look-up table of Figure 6b has been specified. As a result, the resonance matching is compromised, leading to increased transmission. For N = 8, corresponding to a reflection angle of 54.4°, the transmitted power is 11.2% of the incident and the FOM drops to 0.88 (see the Supporting Information). On the other end, when N increases, we get more pronounced phase profile clipping since a larger portion of the 2π phase span needs be covered ($2\pi(N-1)/N$). Consequently, the discretized phase profile starts deviating from being exactly linear and a portion of the incident power is expected to couple to other diffraction orders. However, this effect is not pronounced; even for N = 18, corresponding to a reflection angle of 21.2°, power reflected to other diffraction orders is only 1.7% of the incident and the FOM is as high as 0.97 (see the Supporting Information).

Finally, it should be noted that the designs for anomalous reflection in this section have been based on the "phase-shift" approach. The performance can be exceptionally good, especially for moderate deflection angles and finely discretized phase profiles. We should note, however, that there are known fundamental limitations to this approach which manifest for large deflection angles; approaches to overcome them have been proposed in the literature.[12,40–42] Other strategies for achieving beam steering can include the manipulation of surface states within the concept of leaky-wave antennas.[43,44]

4.4. Focusing Metamirror

Local tunability allows for reconfigurability and different operations with the same design. In this section, we demonstrate focusing. This can be achieved by constructing a reflection phase profile $\varphi_r(y) = \varphi_0 + (2\pi/\lambda_0)[y^2 + f_{pre}^2]^{1/2}$, where f_{pre} is the

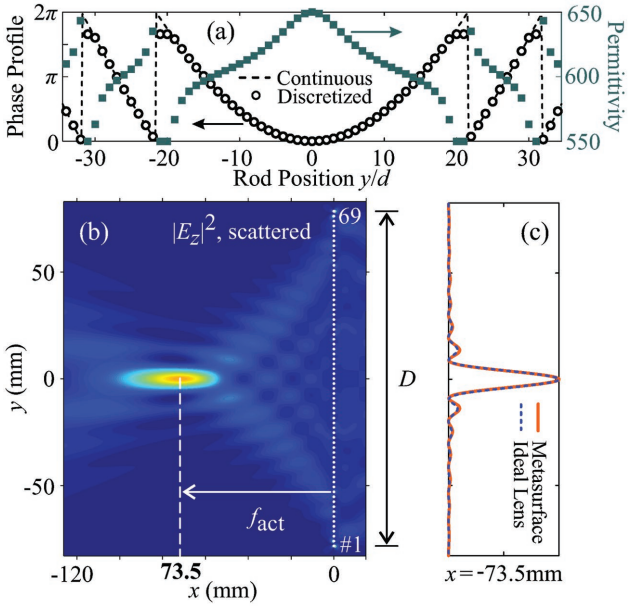

Figure 8. Permittivity-modulated gradient metasurface (a = 0.435 mm, b = 0.196 mm, d = 2.31 mm, N = 69) for beam focusing at f = 20 GHz with a prescribed focal length f_{pre} = 75 mm. a) Required phase profile and rod permittivities. b) Scattered electric field (absolute square). The interference pattern is due to diffraction by the finite lens aperture. The actual intensity maximum is observed at f_{act} = 73.5 mm, slightly different than f_{pre} due to diffraction. c) Comparison of field distribution with a finite ideal classical lens on their common focal plane. The agreement is excellent: the focusing metamirror performs exactly the prescribed phase compensation.

prescribed focal length and φ_0, an arbitrary constant phase. As an example, we select f_{pre} = 75 mm corresponding to only $5\lambda_0$ at 20 GHz. In the Supporting Information an extra focusing scenario of even shorter focal length (30 mm ≈ $2\lambda_0$) is examined. Such low-profile focusing is a distinct advantage of metasurface-based flat lenses compared to conventional bulky counterparts. We use N = 69 meta-atoms, constructing a focusing metamirror with a finite extent $D = Nd$ = 159 mm ≈ $10\lambda_0$. The required phase profile and rod permittivities are depicted in **Figure 8**a. As in Figure 7a, there is some phase clipping due to the finite range of allowed permittivities.

In Figure 8b, we plot the absolute square of the scattered electric field. The reflected energy is focused and a clear focal spot is formed. The interference pattern evident in Figure 8b is caused by diffraction due to the finite extent of the metamirror. It is completely absent when the structure is illuminated with a Gaussian beam of appropriate width instead of a plane wave (see the Supporting Information). The actual focal distance, as defined by the point of maximum intensity along the x-axis, is f_{act} = 73.5 mm. It does not exactly coincide with the prescribed focal distance of the phase compensation (f_{pre} = 75 mm) due to the diffraction effects. This is verified by comparing our proposed metasurface lens with an ideal classical lens of finite aperture. The maximum intensity in the ideal lens case is again found at x = 73.5 mm. Furthermore, the field distributions are almost identical (Figure 8c), verifying that our focusing metamirror performs exactly the prescribed phase compensation.

The performance of the focusing metamirror is further assessed by quantifying the power that is absorbed, transmitted, reflected, and focused by the metasurface as the loss tangent is varied. We calculate the reflected (transmitted) power by integrating the x component of the Poynting vector across the extent D at a distance $-\lambda_0(+\lambda_0)$ from the metasurface. The focused power is found by integrating across the width of the main lobe, which is 18 mm corresponding roughly to one free-space wavelength (15 mm). The results as a percentage of the incident power impinging on the finite aperture are: absorbed, transmitted, reflected, focused power = 1%, 2.7%, 96%, 79.2%, respectively, for tan $\delta = 10^{-4}$; 9.4%, 2.3%, 88%, 72.6%, respectively, for tan $\delta = 10^{-3}$; 53.2%, 1.2%, 45.3%, 37.2%, respectively, for tan $\delta = 10^{-2}$. Furthermore, we define a figure of merit as the ratio of focused to reflected power. It equals 0.825, 0.825, 0.821 for the three loss cases, respectively, verifying that the reflected energy is tightly focused in the main lobe and that loss does not impede the function of phase compensation.

5. Conclusions

In conclusion, we have demonstrated the precise matching of perpendicular electric- and magnetic-nature resonances in metasurfaces made of elliptic dielectric rods. Notably, instead of relying on the fundamental electric dipole resonance as customarily exercised, we have paired the magnetic dipole resonance with a toroidal dipole resonance; this has allowed for the precise matching of both the resonant frequencies and quality factors. Moreover, we have shown that the two resonances remain accurately matched when varying the rod permittivity, which we have exploited for constructing tunable gradient metasurfaces and demonstrating reconfigurable wavefront manipulation.

In this paper, we have demonstrated that despite relying on a pair of matched resonances, the wavefront shaping operations can be performed in reflection instead of transmission. We have shown that this is due to an electric polarizability background, illustrating that it is not always safe to assume that a pair of matched resonances results in perfect transmission. Operating in reflection is beneficial in the context of practical reconfigurable metasurfaces, since any required control circuitry can be accommodated behind the metasurface.

Waveform shaping using low-profile metasurfaces can provide significant technological advantages over bulky conventional lenses. To assess the performance of the proposed metasurfaces, we have focused on a ceramic ferroelectric material (BST) which features high permittivity and ample tunability with external stimuli at gigahertz frequencies and can serve for a first experimental realization; however, high permittivities can also be supplied by polaritonic materials up to tens of terahertz. Tunable beam steering with high efficiencies and tunable beam focusing with ultrashort focal lengths have been shown to be possible even in the presence of moderate dissipative loss.

Supporting Information

Supporting Information is available from the Wiley Online Library or from the author.

Acknowledgements

This work was supported by the European Research Council under ERC Advanced Grant No. 320081 (project PHOTOMETA) and the European Union's Horizon 2020 Future Emerging Technologies call (FETOPEN-RIA) under Grant Agreement No. 736876 (project VISORSURF). Work at Ames Laboratory was supported by the Department of Energy (Basic Energy Sciences, Division of Materials Sciences and Engineering) under Contract No. DE-AC02-07CH11358.

Conflict of Interest

The authors declare no conflict of interest.

Keywords

anomalous reflection, gradient metasurfaces, Mie resonances, toroidal dipole, tunable

Received: May 14, 2018
Revised: August 3, 2018
Published online: September 17, 2018

[1] N. I. Landy, S. Sajuyigbe, J. J. Mock, D. R. Smith, W. J. Padilla, *Phys. Rev. Lett.* **2008**, *100*, 207402.
[2] P. Tassin, L. Zhang, T. Koschny, E. N. Economou, C. M. Soukoulis, *Phys. Rev. Lett.* **2009**, *102*, 053901.
[3] N. Yu, P. Genevet, M. A. Kats, F. Aieta, J.-P. Tetienne, F. Capasso, Z. Gaburro, *Science* **2011**, *334*, 333.
[4] B. Dastmalchi, P. Tassin, T. Koschny, C. M. Soukoulis, *Phys. Rev. B* **2014**, *89*, 115123.
[5] D. L. Sounas, T. Kodera, C. Caloz, *IEEE Trans. Antennas Propag.* **2013**, *61*, 221.
[6] S. Droulias, A. Jain, T. Koschny, C. M. Soukoulis, *Phys. Rev. Lett.* **2017**, *118*, 073901.
[7] O. Tsilipakos, T. Koschny, C. M. Soukoulis, *ACS Photonics* **2018**, *5*, 1101.
[8] S. Kruk, Y. Kivshar, *ACS Photonics* **2017**, *4*, 2638.
[9] W. Liu, Y. S. Kivshar, *Opt. Express* **2018**, *26*, 13085.
[10] M. Decker, I. Staude, M. Falkner, J. Dominguez, D. N. Neshev, I. Brener, T. Pertsch, Y. S. Kivshar, *Adv. Opt. Mater.* **2015**, *3*, 813.
[11] C. Pfeiffer, A. Grbic, *Phys. Rev. Lett.* **2013**, *110*, 197401.
[12] A. Epstein, G. V. Eleftheriades, *J. Opt. Soc. Am. B* **2016**, *33*, A31.
[13] N. M. Estakhri, C. Argyropoulos, A. Alù, *Philos. Trans. R. Soc. A* **2015**, *373*, 20140351.
[14] N. M. Estakhri, A. Alù, *J. Opt. Soc. Am. B* **2016**, *33*, A21.
[15] Y. Yang, W. Wang, P. Moitra, I. I. Kravchenko, D. P. Briggs, J. Valentine, *Nano Lett.* **2014**, *14*, 1394.
[16] V. Asadchy, M. Albooyeh, S. Tretyakov, *J. Opt. Soc. Am. B* **2016**, *33*, A16.
[17] A. Forouzmand, H. Mosallaei, *Adv. Opt. Mater.* **2017**, *5*, 1700147.
[18] X. Liu, K. Fan, I. V. Shadrivov, W. J. Padilla, *Opt. Express* **2017**, *25*, 191.
[19] S. Kruk, B. Hopkins, I. I. Kravchenko, A. Miroshnichenko, D. N. Neshev, Y. S. Kivshar, *APL Photonics* **2016**, *1*, 030801.
[20] Y. Yang, I. I. Kravchenko, D. P. Briggs, J. Valentine, *Nat. Commun.* **2014**, *5*, 5753.
[21] L. Wang, S. Kruk, H. Tang, T. Li, I. Kravchenko, D. N. Neshev, Y. S. Kivshar, *Optica* **2016**, *3*, 1504.
[22] A. Komar, Z. Fang, J. Bohn, J. Sautter, M. Decker, A. Miroshnichenko, T. Pertsch, I. Brener, Y. S. Kivshar, I. Staude, D. N. Neshev, *Appl. Phys. Lett.* **2017**, *110*, 071109.
[23] K. C. Huang, M. L. Povinelli, J. D. Joannopoulos, *Appl. Phys. Lett.* **2004**, *85*, 543.
[24] V. Savinov, V. A. Fedotov, N. I. Zheludev, *Phys. Rev. B* **2014**, *89*, 205112.
[25] T. Kaelberer, V. A. Fedotov, N. Papasimakis, D. P. Tsai, N. I. Zheludev, *Science* **2010**, *330*, 1510.
[26] A. A. Basharin, M. Kafesaki, E. N. Economou, C. M. Soukoulis, V. A. Fedotov, V. Savinov, N. I. Zheludev, *Phys. Rev. X* **2015**, *5*, 011036.
[27] A. C. Tasolamprou, O. Tsilipakos, M. Kafesaki, C. M. Soukoulis, E. N. Economou, *Phys. Rev. B* **2016**, *94*, 205433.
[28] N. Papasimakis, V. A. Fedotov, V. Savinov, T. A. Raybould, N. I. Zheludev, *Nat. Mater.* **2016**, *15*, 263.
[29] O. Tsilipakos, A. C. Tasolamprou, T. Koschny, M. Kafesaki, E. N. Economou, C. M. Soukoulis, *11th International Congress on Engineered Materials Platforms for Novel Wave Phenomena (Metamaterials)*, IEEE, Marseille, France **2017**, https://ieeexplore.ieee.org/document/8107810/.
[30] J.-M. Jin, *The Finite Element Method in Electromagnetics*, John Wiley & Sons, New York **2002**.
[31] O. Tsilipakos, T. V. Yioultsis, E. E. Kriezis, *J. Appl. Phys.* **2009**, *106*, 093109.
[32] L. Peng, L. Ran, H. Chen, H. Zhang, J. A. Kong, T. M. Grzegorczyk, *Phys. Rev. Lett.* **2007**, *98*, 157403.
[33] L. C. Sengupta, S. Sengupta, *Mater. Res. Innovations* **1999**, *2*, 278.
[34] M. Ouaddari, S. Delprat, F. Vidal, M. Chaker, K. Wu, *IEEE Trans. Microwave Theory Tech.* **2005**, *53*, 1390.
[35] B. Slovick, Z. G. Yu, M. Berding, S. Krishnamurthy, *Phys. Rev. B* **2013**, *88*, 165116.
[36] P. Moitra, B. A. Slovick, W. Li, I. I. Kravchencko, D. P. Briggs, S. Krishnamurthy, J. Valentine, *ACS Photonics* **2015**, *2*, 692.
[37] S. Sun, K.-Y. Yang, C.-M. Wang, T.-K. Juan, W. T. Chen, C. Y. Liao, Q. He, S. Xiao, W.-T. Kung, G.-Y. Guo, L. Zhou, D. P. Tsai, *Nano Lett.* **2012**, *12*, 6223.
[38] A. Pors, M. G. Nielsen, R. L. Eriksen, S. I. Bozhevolnyi, *Nano Lett.* **2013**, *13*, 829.
[39] V. S. Asadchy, Y. Ra'di, J. Vehmas, S. A. Tretyakov, *Phys. Rev. Lett.* **2015**, *114*, 095503.
[40] A. Epstein, G. V. Eleftheriades, *Phys. Rev. Lett.* **2016**, *117*, 256103.
[41] V. S. Asadchy, M. Albooyeh, S. N. Tcvetkova, A. Díaz-Rubio, Y. Ra'di, S. A. Tretyakov, *Phys. Rev. B* **2016**, *94*, 075142.
[42] A. Díaz-Rubio, V. S. Asadchy, A. Elsakka, S. A. Tretyakov, *Sci. Adv.* **2017**, *3*, e1602714.
[43] A. C. Tasolamprou, T. Koschny, M. Kafesaki, C. M. Soukoulis, *ACS Photonics* **2017**, *4*, 2782.
[44] S. B. Glybovski, S. A. Tretyakov, P. A. Belov, Y. S. Kivshar, C. R. Simovski, *Phys. Rep.* **2016**, *634*, 1.